Energy &
Environmental
Science

Compositional Heterogeneity in $Cs_yFA_{1-y}Pb(Br_xI_{1-x})_3$ perovskite films and its Impact on Phase Behavior

Journal:	*Energy & Environmental Science*
Manuscript ID	EE-ART-04-2021-001184.R2
Article Type:	Paper
Date Submitted by the Author:	25-Sep-2021
Complete List of Authors:	Barrier, Julien; SSRL, Materials Science Division; École Supérieure de Physique et de Chimie Industrielles de la Ville de Paris Beal, Rachel; SSRL, Materials Science Division; Stanford University Department of Materials Science and Engineering Gold-Parker, Aryeh; SSRL, Materials Science Division; Stanford University Department of Chemistry Vigil, Julian; SSRL, Materials Science Division; Stanford University, Chemical Engineering Wolf, Eli; Stanford University Department of Applied Physics; University of Colorado Boulder, Chemical and Biological Engineering Waquier, Louis; SSRL, Materials Science Division; École Supérieure de Physique et de Chimie Industrielles de la Ville de Paris Weadock, Nicholas; SSRL, Materials Science Division; University of Colorado Boulder, Chemical and Biological Engineering Zhang, Zihan; University of Colorado Boulder Department of Physics Schelhas, Laura; National Renewable Energy Laboratory, Nogueira, Ana Flavia; State University of Campinas, McGehee, Michael; University of Colorado Boulder, Chemical and Biological Engineering; National Renewable Energy Laboratory Toney, Michael; University of Colorado Boulder, Chemical and Biological Engineering

Compositional Heterogeneity in $Cs_yFA_{1-y}Pb(Br_xI_{1-x})_3$ Perovskite Films and its Impact on Phase Behavior

Julien Barrier[1,2,†] Rachel E. Beal[1,3,†] Aryeh Gold-Parker[1,4] Julian A. Vigil[1,5]
Eli Wolf[6,7] Louis Waquier[1,2] Nicholas J. Weadock[1,7] Zihan Zhang[8]
Laura T. Schelhas[9] Ana Flavia Nogueira[10] Michael D. McGehee[7,9]
Michael F. Toney[7*]

[1] SSRL Materials Science Division, SLAC National Accelerator Laboratory, Menlo Park CA 94025, USA
[2] École Supérieure de Physique et de Chimie Industrielles de la Ville de Paris - ESPCI Paris, 75005 Paris, France
[3] Department of Materials Science and Engineering, Stanford University, Stanford CA 94305, USA
[4] Department of Chemistry, Stanford University, Stanford CA 94305
[5] Department of Chemical Engineering, Stanford University, Stanford CA 94305, USA
[6] Department of Applied Physics, Stanford University, Stanford, CA 94305, USA
[7] Department of Chemical and Biological Engineering, University of Colorado Boulder, Boulder, CO 80309, USA
[8] Physics Department, University of Colorado Boulder, Boulder, CO 80309, USA
[9] National Renewable Energy Laboratory, Golden, CO 80401, USA
[10] Institute of Chemistry, University of Campinas, Campinas SP 13083-970 São Paulo, Brazil

Abstract

Hybrid organic inorganic lead halide perovskite semiconductors of the form $Cs_yFA_{1-y}Pb(Br_xI_{1-x})_3$ are promising candidate materials for high-efficiency photovoltaics. Notably, cation and anion substitution can be used to tune the band gaps to optimize performance and improve stability. However, multi-component materials can be prone to compositional and structural inhomogeneity and the extent, length scale and impact of this heterogeneity on lead halide perovskite properties is not well understood. Here we use synchrotron X-ray diffraction to probe the evolution of crystal structure across the tetragonal-to-cubic phase transition for a series of $Cs_yFA_{1-y}Pb(Br_xI_{1-x})_3$ thin films with $x = 0.05$ to 0.3 and $y = 0.17$ to 0.40. We find that the transition occurs across a broad temperature range of approximately 40 °C, much larger than for pure compounds such as $MAPbI_3$ and $MAPbBr_3$. We hypothesize that this smearing of the phase transition is due to compositional inhomogeneities that give rise to a distribution of local transition temperatures and we estimate the composition varies by about 10 % to 15 % with likely greater heterogeneity for the halide anion than the cation. This approach of mapping the transition is a simple and effective method of assessing heterogeneity, enabling evaluation of its impact.

Broader context

This paper focuses on metal halide perovskite thin films, a system of wide interest for photovoltaic applications. Particularly, perovskite films of the form $Cs_yFA_{1-y}Pb(Br_xI_{1-x})_3$ have sparked a lot of enthusiasm for use in tandem solar cell applications since their bandgap is particularly well suited to complement Si. However, these alloyed materials are potentially inhomogeneous, which have implications on the materials properties, including the propensity to photo-induced instability and phase demixing. Stability is one of the most significant challenges faced in these materials before commercialization of solar cell devices. Despite extensive studies, the nature of the inhomogeneities

---

[†] These authors contributed equally.

[*] Correspondance for this work should be addressed to M.F. Toney `michael.toney@colorado.edu`

and the extent of compositional heterogeneity is still not well understood, as there are few simple methods to assess this. It is essential to quantify heterogeneity, particularly at the nanoscale, to understand its impact. Understanding the complex phase behavior is of paramount importance as the phase transitions are around operational temperature of solar devices.

Introduction

Over the last decade, hybrid organic inorganic metal halide perovskites (MHPs) have sparked tremendous enthusiasm due to their favorable optoelectronic properties [1, 2] for applications in both single junction and tandem solar cells as well as other optoelectronic devices [3, 4, 5]. Perovskites have the general chemical formula ABX_3 where for MHPs, A is a monovalent cation, B is a divalent cation, and X is a halide anion. The unit cell comprises corner-sharing BX_6 octahedra that form a cuboctahedral cavity filled by the A-site cation. The perovskite crystal structure accommodates a wide compositional space, and in state-of-the-art MHP photovoltaics, A is typically a mixture of formamidinium ($FA = CH(NH_2)_2{}^+$), methylammonium ($MA = CH_3NH_3{}^+$), and Cs^+, B is typically Pb^{2+}, and X is typically a mixture of I^- and Br^-. Compositional tuning on both the A- and X-site alters the material's band gap, and compositions of the form $Cs_yFA_{1-y}Pb(Br_xI_{1-x})_3$ with $0 < x < 1$ and $0.1 < y < 0.3$ have been found to be particularly well-suited for applications as the top-cell material in tandem perovksite-silicon photovoltaics [6].

Despite the impressive performance of MHP based solar cells, with record efficiencies exceeding 25% and 29% for perovskite and perovskite/Si monolithic tandem devices, respectively [7, 8], there is space for improvement in several aspects before commercialization and widespread deployment becomes feasible [9, 10, 11]. While state-of-the-art MHP solar cells have short circuit current densities that are near theoretical and practical maxima, the open circuit voltage and fill factor can be improved, which could be achieved by suppressing charge carrier recombination in the bulk film and at interfaces. In addition, high-performing multi-cation, multi-halide MHP devices need to be controllably synthesized by cost-efficient and scalable methods. While there is some debate about possible limitations imposed by the toxicity of Pb^{2+}, developing high performing Pb-free solar cells is desirable. Finally, convincingly demonstrating long-term stability remains a key issue [12].

Of these challenges, stability is, arguably, the most important. While thermodynamic stability and chemical decomposition are important, photo-induced instability (or demixing) are a significant challenge for multi-cation, multi-halide MHPs that have wide band gaps needed for tandem photovoltaics. Here illumination induces a nanoscale compositional segregation into I-rich and Br-rich domains [13, 14, 15, 16]. This process requires fast halide anion diffusion that is likely facilitated by high vacancy concentrations [17, 18, 19]. There is some evidence for photoinduced A-site cation demixing as well [20], although mixed A-site MHPs with FA and Cs show improved photo-stability [21]. While the phenomenon of photo-induced phase segregation has been intensively investigated, the mechanism is still under active discussion [16]. It has been suggested that for $\mathrm{MAPb(Br_xI_{1-x})_3}$ perovskites compositions near the tetragonal-to-cubic phase boundary are more optically stable [22]. We have shown that MHP crystallographic phase is not the sole determinant to stability [14], and it has been postulated that initial nanoscale local compositional variations serve as nuclei for the formation of I-rich segregated nanoscale domains under illumination [23, 24, 25]. Furthermore, local compositional fluctuations can impact charge carrier dynamics and device performance [26]. Thus, it is essential to quantify compositional uniformity, particularly at the nanoscale, to understand and control its impact.

Studies have demonstrated optoelectronic and compositional heterogeneity [27, 28, 29] in MHPs across length scales, but almost all investigations have been limited to $>0.1\,\mu\mathrm{m}$ spatial scale [30]. For example, de Quilettes *et al.* showed that photoluminescence (PL) intensities and lifetimes varied between different regions within the same film [27]. Correa-Baena *et al.* used nano-X-ray fluorescence microscopy of mixed halide MHPs to map heterogeneity in I and Br composition showing µm size regions of low Br content but demonstrating improvements in uniformity for some compositions [28]; the same method was used also by Wieghold *et al.* to show that the elemental composition is altered in single grains based on the film thickness and this inhomogeneity explained differences in charge carrier dynamics [26]. Szostak *et al.* mapped chemical diversity of individual regions with nano-spectroscopy [29] showing that these regions have an intrinsic heterogeneity of the organic components. Gratia *et al.* used ion microscopy to map halide composition in $\mathrm{FA_{0.85}MA_{0.15}Pb(Br_{0.15}I_{0.85})_3}$ films at sub-100 nm and observed ≈50 nm regions devoid of Br, and interestingly, noted no evidence for such compositional segregation based on peak broadening in diffraction, an apparent contradiction [31]. Much of the research on heterogeneity is summarized in the review by Tennyson *et al.* [30]. Despite extensive work, easily and accurately quantifying and characterizing compositional heterogeneity remains a significant challenge, especially for 1 to 100 nm length scales.

Compositional heterogeneity can have two origins: intrinsic (or thermodynamic) and extrinsic (processing-induced). The first form is the thermodynamic separation of the multi-component MHP into two or more distinct phases driven by minimization of the free energy. The second likely results from kinetics due to the solution-processing methods used to fabricate MHP materials that may lead to chemical, structural, and electronic property heterogeneity on multiple length scales [30]. Distinguishing these is difficult because the MHP film may be in a kinetically trapped, metastable state. We make no attempt to distinguish intrinsic and extrinsic nonuniformity in this paper and we refer to both as compositional heterogeneity.

To the best of our knowledge, there have been no investigations of the phase behavior and phase diagrams for any multi-cation, multi-halide MHP. This is likely because these are very challenging due to multi-dimensional phase space and the capacity for the perovskite crystal structure to accommodate many different distortions [32] that can make perovskite phase diagrams quite complex. We have mapped the room temperature crystal structures for $\mathrm{Cs_yFA_{1-y}Pb(Br_xI_{1-x})_3}$ thin films with $x = 0.05$ to 0.3 and $y = 0.17$ to 0.40 and identified the cubic-tetragonal solvus [14]. For the simpler four component MHPs, there have been a few reports on phase behavior [33, 34, 35, 20, 36]. For A-site substitution, these have shown limited incorporation of Cs in pseudocubic $\mathrm{Cs_yFA_{1-y}PbI_3}$, about $y = 0.15$ in the bulk powders [33], despite theoretical predictions of much higher solubility ($y = 0.7$) [20]. In contrast, most MHP films show a solubility up to at least $y = 0.3$ for $\mathrm{Cs_yFA_{1-y}PbI_3}$ [37], but these may be kinetically trapped. In $\mathrm{MAPb(Br_xI_{1-x})_3}$, diffraction has shown a miscibility gap up to 350 K with strong intergrowth of I-rich and Br-rich crystallites and observed deviations from Vegard's law [35], a point we discuss later in this manuscript. In $\mathrm{CsPb(Br_xI_{1-x})_3}$, a computational study [38] has predicted a single phase orthorhombic solid-solution at room temperature but phase separate into Br-rich tetragonal and I-rich orthorhombic phases at 50 to 75 °C.

The presence of compositional heterogeneity complicates the phase transition behavior in MHPs, since slight variations in composition can result in a different crystallographic phase being thermodynamically favorable and shift the temperature where structural transitions occur. Because MHPs can undergo phase transitions around operational temperatures, an understanding of their complex phase behavior is necessary. In this work, we explore the nature of the tetragonal-to-cubic phase transition in $\mathrm{Cs_yFA_{1-y}Pb(Br_xI_{1-x})_3}$ perovskites and how these behaviors differ from those observed in pure compounds such as $\mathrm{MAPbI_3}$ and $\mathrm{MAPbBr_3}$. Crystal structure and phase transitions are characterized using X-ray diffraction (XRD), and the temperature dependence of the band gap is determined from the external quantum efficiency (EQE) of optimized devices.

We track the lattice parameter and the octahedral tilt angle across the transition and use the octahedral tilt angle to characterize the evolution of the crystal structure from tetragonal into cubic. We find that that this transition occurs over a broad temperature range, and we also observe a change in the temperature dependence of the band gap near the temperature range where the MHP structure becomes cubic. The importance of this study is that we show that photovoltaic-relevant MHP films can be compositionally heterogeneous at the nanoscale and we establish a simple methodology to characterize this heterogeneity.

Results

We investigate a series of $\mathrm{Cs_yFA_{1-y}Pb(Br_xI_{1-x})_3}$ films with $x = 0.05$, 0.17, 0.2 or 0.3 and with $y =$ 0.17, 0.25 or 0.4 that have well-controlled, and nearly constant morphology. Details on the film preparation are given in ref. 14 and in the Experimental Section below.

Structural considerations

First, we briefly recall structural stability considerations. The degree of distortion from the cubic perovskite crystal structure and hence the tendency to form non-cubic structures can be described by the Goldschmidt tolerance factor, τ_G, which has the equation:

$$\tau_G = \frac{r_A + r_X}{\sqrt{2}(r_B + r_X)} \tag{1}$$

where r_i is the ionic radius of ion i [39]. Effectively, the Goldschmidt tolerance factor captures the size mismatch between the A-site cation and the cuboctahedral cavity formed by the $\mathrm{BX_6}$ octahedra, assuming all of the ions are hard spheres. A τ_G greater than 1 indicates that the A-site cation is too large for the cuboctahedral cavity and eventually leads to the formation of a non-perovskite phase. On the other hand, a τ_G less than 1 indicates that the A-site cation is too small, which causes the $\mathrm{BX_6}$ octahedra to tilt in order to reduce the size of the cuboctahedral cavity. Fifteen symmetrically distinct tilt patterns are possible for $\mathrm{ABX_3}$ perovskites depending on the size and properties of the atoms comprising the material and their interactions [40].

These tilt patterns are codified with Glazer notation [41] and can describe cubic, tetragonal, and orthorhombic perovskite crystal structures [42, 43, 44, 45, 46]. In this notation, the letters *a*, *b*, and *c* indicate the magnitude of rotation about the x-, y-, and z-axes, respectively, in the direction indicated by the superscript. A "0" superscript indicates no rotation, so the $Pm\overline{3}m$ cubic crystal structure is denoted $a^0a^0a^0$. Successive octahedra along an axis can either rotate in the same (in-phase) or opposite (out-of-phase) directions. A "+" superscript indicates in-phase rotation of equal magnitude of the octahedra along the specified axis, whereas a "$-$" superscript indicates that successive octahedra along that axis are rotated equally in magnitude but in opposite directions. Tilt patterns that result in a structure with both in-phase and out-of-phase tilts that are equal in magnitude are termed antidistorted [47, 48]. In an antidistortive phase transition from an untilted to a tilted structure, the size of the unit cell increases, but centrosymmetry is preserved [47]. Tetragonal-to-cubic phase transitions in metal-halide perovksites are antidistortive.

While the Goldschmidt tolerance factor is a good indicator for the formation of either perovskite or non-perovskite phases, it cannot be used to predict the predominance of a given crystal structure within the perovskite family. Bartel *et al.* [49] have developed an alternative to the conventional Goldschmidt tolerance factor, and in Supplementary section 1, we discuss the ability of tolerance factors from Bartel *et al.* [49] and Goldschmidt to predict crystal structure within the perovskite family.

Figure 1a shows the XRD patterns for two different $Cs_yFA_{1-y}Pb(Br_xI_{1-x})_3$ compositions at room temperature compared with $MAPbI_3$. This figure shows that $Cs_{0.17}FA_{0.83}Pb(Br_{0.4}I_{0.6})_3$ has a cubic perovskite structure (untilted $a^0a^0a^0$ in Glazer notation), while $Cs_{0.4}FA_{0.6}Pb(Br_{0.17}I_{0.83})_3$ has a tetragonal $P4/mbm$ structure that arises from in-phase tilting of the PbX_6 octahedra (denoted $a^0a^0c^+$). These structures are visualized in figure 1b and figure 1c, respectively. XRD data for $MAPbI_3$, which has a tetragonal $I4/mcm$ structure, is also shown. As previously mentioned, the PbI_6 are tilted out-of-phase ($a^0a^0c^-$) as shown in figure 1d. While both of these structures are antidistorted, they are crystallographically distinct. In tetragonal $Cs_yFA_{1-y}Pb(Br_xI_{1-x})_3$ perovskites, neighboring PbX_6 octahedra in a given (001) plane have the opposite sense of rotation, but each (001) plane is identical. In $MAPbI_3$ the arrangement of PbX_6 octahedra in a given (001) plane is similar, but the sense of rotation alternates between each successive plane. In addition to $MAPbI_3$, many oxide perovskites also have the $I4/mcm$ space group and out-of-phase tilt pattern in the tetragonal phase [51, 52, 53, 54]. Note that the in-phase tilt pattern is consistent with previous works on MHPs comprising either

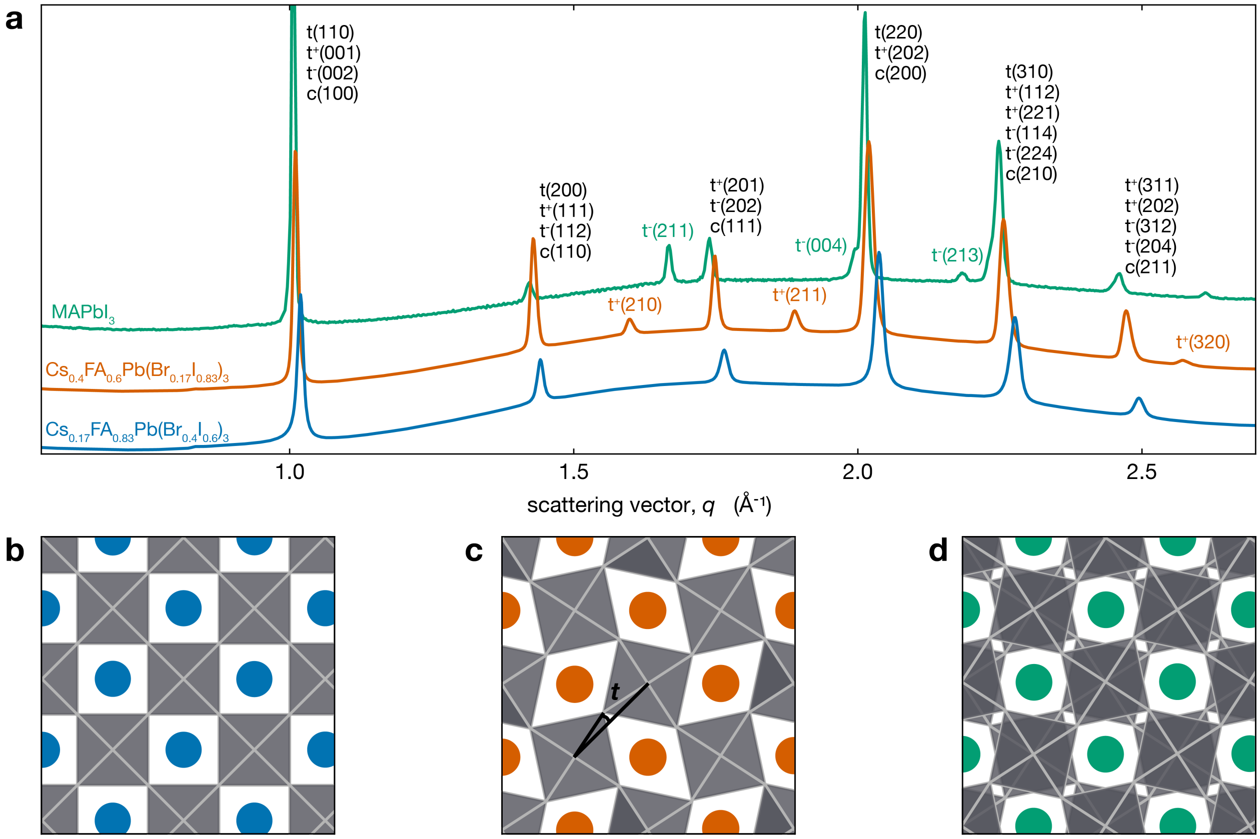

Figure 1: (a) XRD patterns for different $\mathrm{Cs_yFA_{1-y}Pb(Br_xI_{1-x})_3}$ compositions exhibiting both tetragonal $\mathrm{a^0a^0c^+}$ (tetragonal peaks indexed with t^+) and cubic $\mathrm{a^0a^0a^0}$ structures as well as the $\mathrm{a^0a^0c^-}$ phase of $\mathrm{MAPbI_3}$ ($\mathrm{MAPbI_3}$ data from Schelhas *et al.* [50]). The y-axis is linear in intensity (arbitrary units not shown) with an offset between the three patterns. Views of (b) $\mathrm{a^0a^0a^0}$, (c) $\mathrm{a^0a^0c^+}$, and (d) $\mathrm{a^0a^0c^-}$ structures looking down the c-axis. Blue, orange and green spheres represent the A-site cation, and the $\mathrm{PbX_6}$ octahedra are shown in grey. The tilt angle t we consider here is the angle between the black lines in (c)

inorganic or FA cations [55, 56, 57, 14, 58, 33, 59]

For $\mathrm{Cs_{0.4}FA_{0.6}Pb(Br_{0.17}I_{0.83})_3}$, the symmetry associated with in-phase tilting of the $\mathrm{PbX_6}$ octahedra results in the emergence of several tetragonal superlattice peaks, including the $t(210)$ and $t(211)$ reflections around 1.6 and 1.9 $\mathrm{\AA}^{-1}$, respectively, which are not observed in cubic $\mathrm{Cs_{0.17}FA_{0.83}Pb(Br_{0.4}I_{0.6})_3}$. We note that a tetragonal phase should result in the splitting of the cubic $c(100)$ peak into $t(110)$ and $t(001)$ reflections and the $c(200)$ into $t(220)$ and $t(002)$. The difference in tetragonal peak positions is expected to be about 0.5 % at room temperature. However, the observed XRD peak full width at half maximum (FWHM) for the $t(110)$-$t(001)$ and $t(220)$-$t(002)$ peaks is about three times larger than this expected splitting of 0.5 % and hence does not allow us to resolve two separate peaks from this measurement.

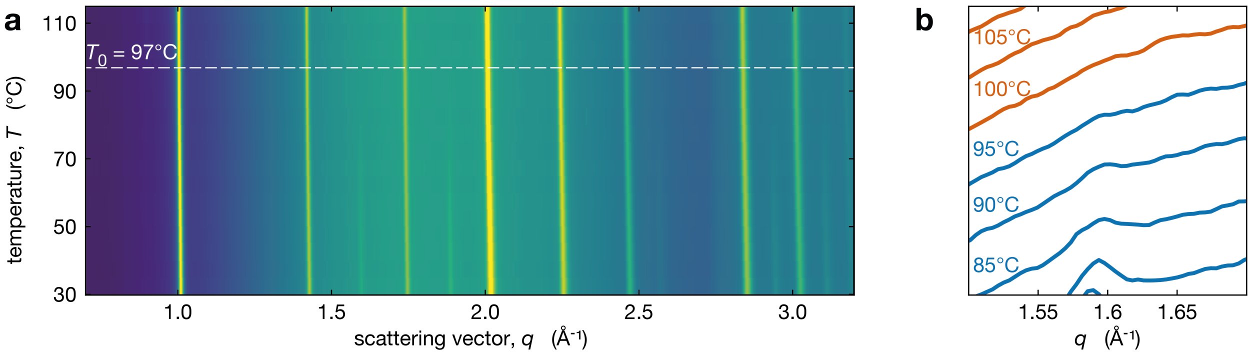

Figure 2: a) Temperature XRD map for $Cs_{0.4}FA_{0.6}Pb(Br_{0.17}I_{0.83})_3$ with the extracted T_0 (temperature where film is purely cubic) indicated by a dashed line. b) Evolution of the integrated intensity of the $t(210)$ superlattice peak. Temperature is increasing moving up in the vertical direction. The y-axis is linear and represents the intensity counts in arbitrary units.

Phase transition monitored through the disappearance of tetragonal reflections

We performed in situ XRD on the series of perovksite thin films while heating through the tetragonal-to-cubic phase transition. The temperature dependent XRD patterns in $Cs_{0.4}FA_{0.6}Pb(Br_{0.17}I_{0.83})_3$ are shown in figure 2a, and figure 2b shows the region near the $t(210)$ peak demonstrating the disappearance of this tetragonal superlattice peak with increasing temperature. The $t(210)$ peak is weak but observable at 95 °C, but it is not observed at 100 °C. At all temperatures, the XRD peaks have been fit with a Voigt function over a quadratic background from the substrate. Because small peaks are hard to distinguish from background and noise, we used chi-squared analysis to determine the presence of tetragonal reflection at each temperature. All calculations and fitting procedures are explained in greater detail in Supplementary section 2. We identify the temperature where the tetragonal peak intensities go to zero as T_0. For $Cs_{0.4}FA_{0.6}Pb(Br_{0.17}I_{0.83})_3$ (figure 2) this is 97(3) °C (See Supplementary section 2 for details). We note that T_0 may represent a solidus temperature [14] where above T_0, the MHP film is in a fully cubic crystal structure but below this, there exist tetragonal domains.

Behaviour of the phase transition

To track the phase transition behavior of $Cs_yFA_{1-y}Pb(Br_xI_{1-x})_3$ perovskite films, we extract the average octahedral tilt angle t from the tetragonal reflection intensities in our XRD measurements (see Supplementary section 3). Note that we define the tilt angle for one PbX_6 octahedron, with

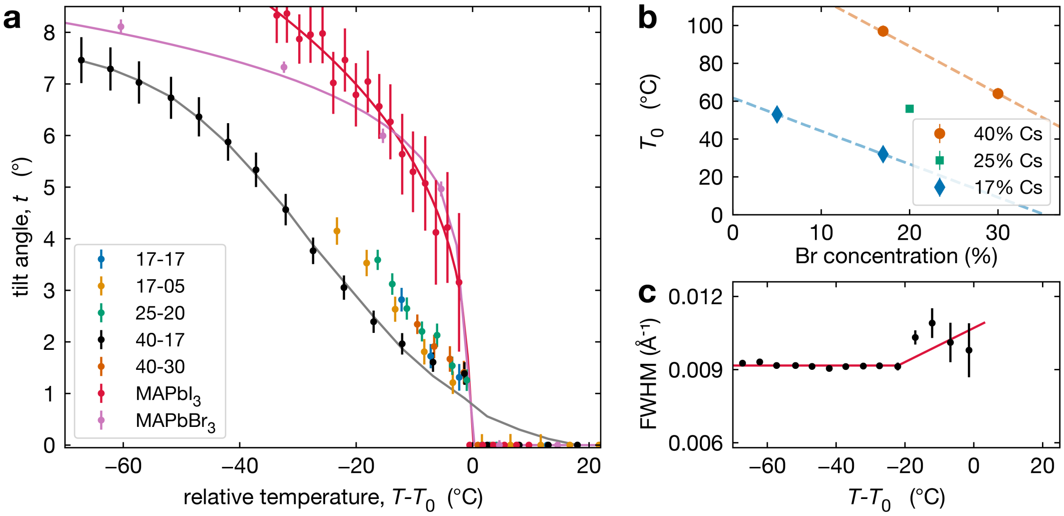

Figure 3: a) Octahedral tilt angle (symbols) plotted as a function of temperature for all compositions studied with data for $MAPbI_3$ thin films extracted from Schelhas *et al.* [50] and $MAPbBr_3$ single crystals. The solid lines show fits to these data as explained in the text. b) Temperature T_0 as a function of Br concentration at constant Cs compositions: 17% (blue diamonds), 25% (green square), 40% (red dots). c) The FWHM of the $t(210)$ peak in $Cs_{0.4}FA_{0.6}Pb(Br_{0.17}I_{0.83})_3$ increases slightly around 20 °C below T_0.

Pb taken as the center, and the angle is relative to the cubic phase atomic position of the halide (see figure 1c). This is the tilt angle *averaged* over space and time. Hence, if the MHP film is heterogeneous, either because of extrinsic compositional variations or due to the coexistence of cubic and tetragonal phases, t is averaged over these regions. As explained in Supplementary section 3, the presence of preferred orientation in our $Cs_yFA_{1-y}Pb(Br_xI_{1-x})_3$ perovskite films results in some uncertainty in the absolute value of the tilt angle. This would manifest as a systematic change in the magnitude of the tilt angle (e.g., shifted higher or lower by some constant multiplier) but will not impact our conclusions, as relative changes are not affected.

The temperature evolution of the tilt angle, t, is shown in figure 3a for all $Cs_yFA_{1-y}Pb(Br_xI_{1-x})_3$ compositions along with comparable tilt angle temperature dependence for pure compounds, including $MAPbI_3$ films [50] and $MAPbBr_3$ single crystals. To aid comparison, we have plotted t as a function of $T - T_0$, where for $Cs_yFA_{1-y}Pb(Br_xI_{1-x})_3$ films T_0 is the temperature where the average tilt goes to zero, and for $MAPbI_3$ films and $MAPbBr_3$, T_0 is the phase transition temperature. The results shown in figure 3a for $MAPbI_3$ and $MAPbBr_3$ are consistent with the literature [60, 61, 62, 63, 59]. The striking qualitative observation from figure 3a is that the tilt evolution at the transition in all the mixed A-site, halide $Cs_yFA_{1-y}Pb(Br_xI_{1-x})_3$ compositions is significantly broadened compared to $MAPbI_3$ films and $MAPbBr_3$, which as we explain below, is a manifestation of compositional heterogeneity. This behavior is most apparent for 40-17 and 17-05 where we have the largest temperature range. For all our alloyed compositions, figure 3a shows that the slopes of the tilt angle t versus temperature T are much smaller than it is for the pure compounds $MAPbI_3$ and $MAPbBr_3$, consistent with the broadened transition although there is a few °C offset in the tilt for 17-17, 25-20 and 40-30 (compared to 40-17), reflecting the errorbar in determining T_0. For some compositions (17-17, 25-20 and 40-30), the temperature range is limited since we are unable to cool the films.

As noted in the introduction, we do not distinguish between intrinsic (thermodynamic phase coexistence) and extrinsic compositional heterogeneity. Hence, we model the phase transition behavior in figure 3a as a smeared first order or second-order transition. For a first order behavior, the intrinsic temperature dependence is a step function at T_c; while for the second-order transition, the behavior near the transition follows a power-law of the form $t \sim (T_c - T)^\beta$, where β is the critical exponent for the phase transition and T_c is the transition temperature. For either type of transition, we account for the impact of compositional heterogeneity by convoluting the intrinsic temperature dependence (step function or power-law) with a Gaussian distribution of transition temperatures. Both fitting processes are discussed in detail in Supplementary section 4. For $Cs_{0.4}FA_{0.6}Pb(Br_{0.17}I_{0.83})_3$, the step function and power-law fits give a T_c at 73 °C and 80 °C, respectively, with a broad width due to the distribution of transition temperatures (52 °C and 45 °C, respectively). The best fit value for β is 0.49, but with large uncertainty. We observe qualitatively similar behavior in all of the $Cs_yFA_{1-y}Pb(Br_xI_{1-x})_3$ compositions studied and report T_c, fitting transition width, and T_0 values in table 1, while figure 3b plots T_0 for different compositions. Note that our experimental data set only allows us to determine a T_c and transition width for $Cs_{0.4}FA_{0.6}Pb(Br_{0.17}I_{0.83})_3$ and $Cs_{0.17}FA_{0.83}Pb(Br_{0.05}I_{0.95})_3$, as data are only available above room temperature and for $Cs_{0.17}FA_{0.83}Pb(Br_{0.05}I_{0.95})_3$, we can only set a lower limit on the transition width of 21 °C.

This behaviour is different from pure compounds, $MAPbI_3$ and $MAPbBr_3$. Despite being a well-studied system, the character of the tetragonal-to-cubic phase transition in $MAPbI_3$ is still debated. DFT calculations suggest that the transition is second-order [64], but several experimental studies have concluded that the transition is closer to tricritical (mean field exponent $\beta = 0.25$) [60, 62, 63, 65]. A recent study of the tetragonal-to-cubic transition in a deuterated $MAPbI_3$ single crystal indicates that the transition is at least weakly first order with small tetragonal domains nucleating

Table 1: Phase transition temperatures T_c and T_0 and fitting temperature transition width for the smeared first order behavior, for the compositions studied herein. Note that for $y = 17$, $x = 5$, the limited temperature range may result in an overestimated T_c and underestimated transition width.

[Cs], y (%)	**[Br], x (%)**	T_0 **(°C)**	T_c **(°C)**	**transition width (°C)**
17	05	53	39	> 21
17	17	37		
25	20	56		
40	17	97	73	45
40	30	64		

near iodide vacancies in the cubic lattice [66].

For $Cs_yFA_{1-y}Pb(Br_xI_{1-x})_3$, we observe a very small increase in the FWHM of the $t(210)$ Bragg peak about 10 to 20 °C below T_0, as shown in figure 3c. This weak dependence is, in general, inconsistent with the expected power-law increase in FWHM [67] for a second-order transition. This observation suggests that the tetragonal-to-cubic transition in our $Cs_yFA_{1-y}Pb(Br_xI_{1-x})_3$ films is not second order.

Lattice parameter behavior

The temperature dependence of the lattice parameters through the phase transition provides insight into the phase behavior and nature of the heterogeneity that broadens the transition. Figure 4a shows the temperature evolution of the lattice parameters a' and c as well as the pseudo-cubic lattice parameter d for $Cs_{0.4}FA_{0.6}Pb(Br_{0.17}I_{0.83})_3$ and $Cs_{0.17}FA_{0.83}Pb(Br_{0.05}I_{0.95})_3$. We used the $t(210)$ and $t(201)$ peaks to extract the lattice parameters, and for ease of comparison, we plot $a' = a/\sqrt{2}$ and $d = (a'^2c)^{\frac{1}{3}}$. These lattice parameters are thus reflective of only the regions that are tetragonal within the film. It is informative to compare this dependence to that for the pure compound $MAPbI_3$ [60], which is shown in figure 4b, and behaves the same as the pure compound $MAPbBr_3$ [61]. Before making this comparison, we calculate that the volumetric thermal expansion coefficients (β_V) for $Cs_{0.4}FA_{0.6}Pb(Br_{0.17}I_{0.83})_3$ and $Cs_{0.17}FA_{0.83}Pb(Br_{0.05}I_{0.95})_3$ as $(2.11\pm0.1)\times10^{-4}K^{-1}$ and $(1.83\pm0.3)\times10^{-4}K^{-1}$, respectively. These values are slightly larger than $\beta_V = (1.52\pm0.07)\times10^{-4}\ K^{-1}$ for $Cs_{0.15}FA_{0.85}PbI_3$[68], and suggest that Br in the X site gives a larger β_V compared to I. We observe no change in β_V at the phase transition (T_0 in figure 4a).

There is a distinct difference in the lattice parameter behavior near the transition for $Cs_yFA_{1-y}Pb(Br_xI_{1-x})_3$ and $MAPbI_3$ in that for the pure compound a' and c converge approaching the transition temperature, but for the mixed-cation, mixed halide perovskite a' and c diverge approaching T_0, especially c. We

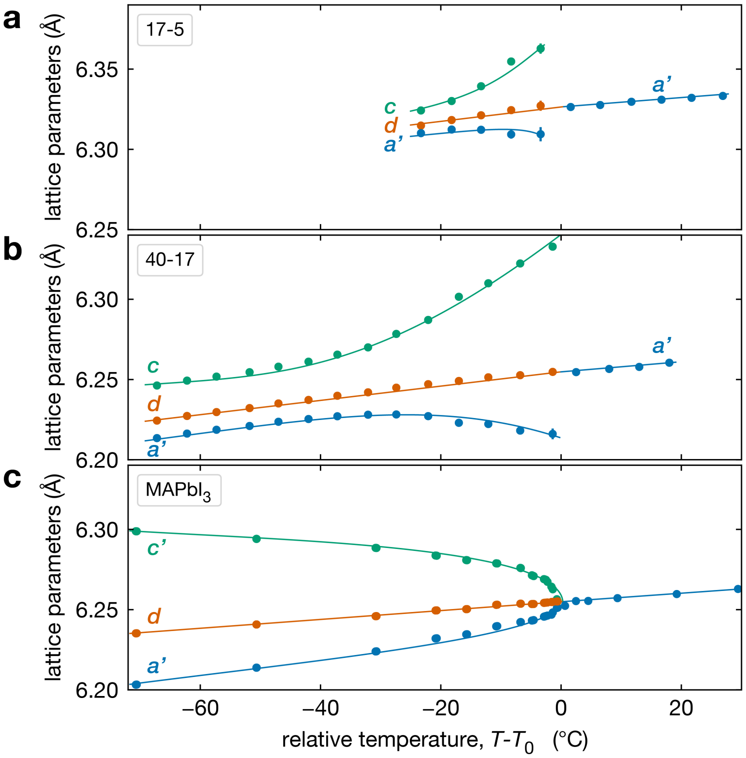

Figure 4: Evolution of lattice parameters for $Cs_{0.17}FA_{0.83}Pb(Br_{0.05}I_{0.95})_3$ (a), $Cs_{0.4}FA_{0.6}Pb(Br_{0.17}I_{0.83})_3$ (b) and $MAPbI_3$ (c) plotted as a function of the relative temperature $T - T_0$. (a-b) The parameters are extracted from the tetragonal peak positions. c) Data extracted from ref [60]. Here $a' = a/\sqrt{2}$ (blue), $d = (a'^2 c)^{\frac{1}{3}}$ (brown) and c (green). For $MAPbI_3$ we plot $c' = c/2$ instead. Above T_0, the structure is cubic, so only a single lattice parameter is shown. Solid lines show the general trend.

propose the following explanation for this unusual observation for $Cs_yFA_{1-y}Pb(Br_xI_{1-x})_3$ perovskite films. This divergent behavior is a manifestation of the compositional heterogeneity and the resulting distribution of transition temperatures. Figure 3c and Table 1 show that $Cs_yFA_{1-y}Pb(Br_xI_{1-x})_3$ with high Br and/or low Cs will transform into the cubic phase at lower temperatures than for low Br and/or high Cs. Consequently, as temperature increases, regions of the $Cs_yFA_{1-y}Pb(Br_xI_{1-x})_3$ films with high Br and/or low Cs will transform first into the cubic phase and the tetragonal regions of the film will be those that are richer in Cs or poor in Br. Since the tetragonal $t(210)$ and $t(201)$ peaks are used to determine a' and c in figure 4a, these lattice parameters will increasingly correspond to regions of low Br and/or high Cs. Figure 4a shows c increasing approaching T_0, and these still tetragonal regions must have relatively more I, the larger halide, thus driving the larger c. Although indirect, this suggests that there is more heterogeneity in the halide composition than for the A-site cation. We expand on this hypothesized behavior in Supplementary section 5 with a simple model with four regions will different compositions. Overall, these observations on the lattice parameters support our conclusion on compositional heterogeneity broadening the transition and point to the halides as more heterogeneous.

Band gap temperature dependence

To better understand how this tetragonal-to-cubic transition might influence the operation of solar cells, we measured the optical band gap as a function of temperature. We measured the external quantum efficiency (EQE) of an optimized $Cs_{0.17}FA_{0.83}Pb(Br_{0.17}I_{0.83})_3$ device at three temperatures on either side of T_0 (temperature where the material is fully cubic) and extracted the band gap by fitting the low energy tail of the EQE at each temperature (see Supplementary section 6). The extracted optical band gaps are plotted in figure 5. We observe that below T_0 the band gap decreases with temperature, and above T_0, the band gap increases with temperature. While both trends are modest, they are distinguishable.

In the low-temperature tetragonal phase, the average tilt angle decreases upon heating, increasing the overlap of the orbitals associated with the Pb−X bonds, decreasing the band gap [69, 70, 71, 72], consistent with figure 5. In the cubic phase above T_0, the band gap increases with temperature, consistent with DFT calculations that show that the band gaps of biaxially strained cubic $CsPbI_3$ and $CsSnI_3$ increase with strain [70]. This is because in the cubic phase, lattice expansion reduces the orbital overlap, increasing the band gap [69, 70, 71, 72].

We fit the decreasing and increasing band gap regimes with linear dependence and find that their intersection at 38 °C is nearly identical to the value of $T_0 = 37\,^{\circ}\mathrm{C}$ that we estimate from XRD data, see figure 3b. These results (figure 5) coupled with our map of the transition temperature (figure 3b) can be used to estimate the temperature where the slope in the band gap vs temperature changes from negative to positive (between about T_c and T_0). A positive slope for the band gap vs temperature results in a comparatively more efficient solar cell at higher temperatures than for a negative slope. Thus, the temperature where this slope changes may have important implications for the temperature coefficient for power conversion efficiency in MHP solar cells, if this is near typical operational temperatures.

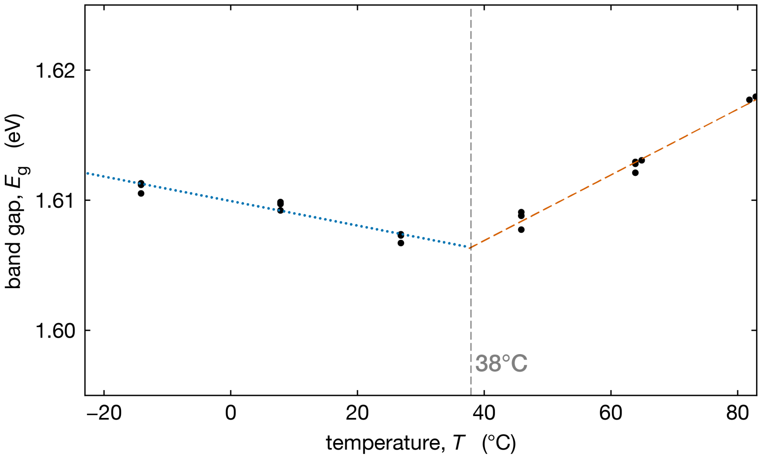

Figure 5: Band gap (eV) (black dots) for perovskite composition $Cs_{0.17}FA_{0.83}Pb(Br_{0.17}I_{0.83})_3$ as a function of temperature (°C), calculated from up and downward cycles of EQE, with a linear fit before discontinuity (blue dashed line) and after slope discontinuity (red dotted line). The grey dashed line shows the intersection of the two slopes.

Discussion

Relative to the pure phases, we have observed two distinct differences in the phase transition behavior for multi-cation, multi-halide MHPs. First, as reflected in the octahedral tilt angle, the transition is broadened over a considerable temperature range of the order of 40 °C. Second, the behavior of the lattice parameters of the tetragonal domains just below the transition diverges slightly as opposed to converging in the pure compounds. These behaviors are consistent with the presence of compositional heterogeneity.

With respect to the phase transition behavior, we have defined two characteristic temperatures. T_0 is the temperature at which the average tilt angle becomes zero and the entirety of the film adopts the cubic structure. T_c is the average transition temperature obtained from fitting the temperature dependence of the tilt angle to a broadened transition. While we cannot distinguish compositional heterogeneity as intrinsic (or thermodynamic) or extrinsic (processing-induced), T_0 and T_c have different meanings for these scenarios. For the case of two-phase coexistence, with increasing temperature, the film evolves from pure tetragonal to cubic plus tetragonal to pure cubic [38]. Here, T_0 is a solvus temperature, while T_c is near the middle of the two-phase region. In the case of extrinsic heterogeneity, T_0 corresponds to the transition temperature for regions with the highest transition temperature and T_c is the transition temperature reflective of the average composition. In either case the breadth of the transition, as obtained from either the fit transition width (See Supplementary section 2.3) or the difference between T_0 and T_c, is indicative of the compositional heterogeneity and can be used to provide an estimate of these inhomogeneities. With reference to figure 3b, which shows the variation in T_0 with Cs and Br composition, a 30 to 40 °C change corresponds to roughly 10 to 15 % variation in either Cs or Br composition. This suggests compositional variation of the order 10 to 15 %, which is considerable.

There are additional ways that the phase transition might be broadened, in particular, the compound can be relaxor ferroelectric or dipolar glass. In this case, a homogeneous solid solution would transform upon cooling from a non-polar paraelectric to an ergodic relaxor state with polar nanoregions. This can eventually lead to vanishing or quenching the phase transition [73]. While some studies pointed out that MHP alloys can present these responses [74, 75], this is not the case in our work because (a) the P4/mbm tetragonal phase is not consistent with an ergodic relaxor or dipolar glass [73], (b) there is no evidence of ordered A or X sites, (c) at the temperature of our experiments (>300 K), freezing out-of-rotational motions in the organics does not occur and (d) we constantly observe a phase transition throughout our compositional space

From figure 3b, we find that at fixed Br substitution, T_0 increases with increasing Cs substitution, and at fixed Cs substitution, T_0 decreases with increasing Br substitution. The room temperature phase map reported by Beal *et al.* suggests that for higher degrees of Cs substitution, more Br substitution is required before any tetragonal phase is observed [14]. This is because Cs is a smaller cation than FA, and Br is a smaller anion than I. Structurally, Br substitution shrinks the size of the cuboctahedral cavity so that it is a better fit for Cs, and the Goldschmidt tolerance factor τ_G is closer to unity [39]. Thus, when the amount of Br in the lattice is increased, more Cs can be substituted into the cubic crystal lattice before any distortion in the form of octahedral rotations is required to decrease the size of the cuboctahedral cavity [14]. This structural argument is also supported by DFT calculations, which confirm that the energy of the tetragonal phase is lower in systems where the A-site cation is small relative to its cuboctahedral cavity ($\tau_G < 1$) [55].

A compositional variation of 10 to 15 % is significant. It is reasonable to expect that this should lead to broadening of the XRD peaks of the order 0.5 to 1 % of the peak Q value (e.g., $0.005\,\text{Å}^{-1}$ - $0.01\,\text{Å}^{-1}$ for the $t(110)/(002)$ peak). This is estimated from the variation in lattice parameters with composition [35, 37] and the compositional differences estimated above. This prediction is less than the observed XRD peak widths of the $t(110)/(002)$ and $t(200)/(112)$ fundamental XRD peaks of about $0.005\,\text{Å}^{-1}$ and $0.006\,\text{Å}^{-1}$, respectively. One explanation of this apparent discrepancy is that regions of different composition are partly coherently strained to have similar or equal lattice parameters throughout the film; this would imply that the regions with varied composition are small in order to achieve such lattice coherency. This explanation would result in smaller peak widths than predicted from the estimated compositional variations, consistent with our data. In $\mathrm{MAPb(Br_xI_{1-x})_3}$, prior work has shown a miscibility gap with strong intergrowth of I-rich and Br-rich crystallites and unexpected deviations from Vegard's law [35]. These observations also may be related to the possibility of coherency strain.

Conclusion

We used synchrotron XRD to characterize the crystal structure of $\mathrm{Cs_yFA_{1-y}Pb(Br_xI_{1-x})_3}$ perovskites across the tetragonal-to-cubic phase transition. We find that, in contrast to $\mathrm{MAPbI_3}$, which has an out-of-phase octahedral tilt pattern, $\mathrm{Cs_yFA_{1-y}Pb(Br_xI_{1-x})_3}$ perovskites have an in-phase pattern of octahedral rotations about the *c*-axis. This symmetry gives rise to superlattice reflections in the XRD patterns that we use to calculate the temperature dependence of the octahedral tilt angle and lattice parameters across the transitions. Our results show that the tetragonal to cubic transition occurs over a broad range of temperatures that we identify as due to compositional heterogeneity leading to coexisting cubic and tetragonal regions. These give rise to a range of local transition temperatures that effectively smear out into the global transition. We estimate the local compositional variations of about 10 to 15 % in either or both FA/Cs and Br/I, although the data suggest more in the halide. We also find that the temperature dependence of the band gap changes sign from negative to positive near the temperature where the MHP structure becomes cubic, which is explained as a competition between lattice expansion and lead-halide bond length changes due to varying tilt angle.

Our results support and complement previous works demonstrating that multi-anion, multi-cation MHP films can be compositionally heterogeneous at the nanoscale. Furthermore, we have established a simple methodology to characterize this compositional heterogeneity in mixed anion, cation MHP. Using this methodology can enable a way to understand the extent and impact of heterogeneity on the properties and performance of MHP photovoltaic materials.

Experimental data

Device fabrication & characterisation Films were prepared using the standard chlorobenzene antisolvent method with in a 4:1 dimethylformamide (DMF)/dimethyl sulfoxide solvent (DMSO) mixture that was optimized for film morphology at each composition and is detailed in ref [14]. After spin casting, films were annealed on a hotplate at 60 °C for 1 min and subsequently at 105 °C for 30 min under an N_2 atmosphere. Two-dimensional X-ray scattering was collected with monochromatic 12.7 keV synchrotron beam and recorded on $255\,\mathrm{mm}^2 \times 255\,\mathrm{mm}^2$ detector, under a flowing He atmosphere. Images were calibrated using LaB_6 and integrated to 1D using PyFAI[76]. Tilt angle was obtained following the method developed in Supplementary sections 2 and 3. EQE was measured in a cryostat on solar cells made with the following stack: Glass, ITO, NiOx, Perovskite, PCBM, ALD SnO_2, Sputtered ITO. Light was shone through the Sputtered ITO side.

$MAPbBr_3$ crystallization and single crystal X-ray diffraction $MAPbBr_3$ crystals were prepared by inverse temperature crystallization. A 1 M solution of $PbBr_2$ and MABr in DMF was prepared and passed through a 0.22 µm filter; the filtered solution was heated to 82 °C in an oil bath and removed after 30 min. $MAPbBr_3$ crystals were isolated quickly from the cooling mother liquor to avoid re-dissolution. Crystals were mounted on an X-ray transparent MiTeGen microloop using Paratone oil and single crystal X-ray diffraction was performed on a Bruker D8 Venture diffractometer equipped with a Photon 100 CMOS detector. The temperature was varied from 100 to 300 K with an Oxford Cryostream.

Data were collected from ϕ and ω scans using Mo-Kα radiation ($\lambda = 0.710\,73$ Å). The frames were integrated using SAINT V8.38A and absorption correction was performed with SADABS-2016/2, both implemented in the Bruker APEX 3 software. Space group determination was performed with XPREP, with space group assignment based on reported structures, systematic absences, $|E * E - 1|$ statistics, and refinement statistics. The structure was solved using direct methods with the SHELXT software [77] and refined using a least-squares method implemented by SHELXL-2014/7 in the Olex 2 software package.

The Pb and Br thermal displacement parameters are refined anisotropically, whereas the C, N, and H parameters are refined isotropically. Due to the well-known dynamic cation disorder in the tetragonal and cubic phases, the methylammonium (MA) molecule was refined two ways: as a single atom centered in the interstices, or as a molecule confined to reside along high symmetry directions determined by residual electron densities. Additional constraints to the MA cation were applied to the C−−N bond length (1.47 Å) and to fix fractional occupancy to maintain stoichiometry. No significant differences were observed in the final structures refined with these two methods.

Conflicts of interest There are no conflicts of interest to declare

Acknowledgements This work was supported by the U.S. Department of Energy (DOE) Solar Energy Technology Office (SETO) of the Energy Efficiency and Renewable Energy (EERE) award for the Derisking Halide Perovskite Solar Cells project at the National Renewable Energy Laboratory under Contract No. DE-AC36-08-GO28308 managed and operated by the Alliance for Sustainable Energy, LLC. Use of the Stanford Synchrotron Radiation Light-source, SLAC National Accelerator Laboratory, is supported by the U.S. Department of Energy, Office of Science, Office of Basic Energy Sciences under Contract No. DE-AC02-76SF00515. Part of this work was performed at the Stanford Nano Shared Facilities (SNSF), supported by the National Science Foundation under award ECCS-2026822. J.B. is supported by Fonds ESPCI Paris. J.A.V. acknowledges fellowship support from the Stanford University Office of the Vice Provost of Graduate Education and the National Science Foundation Graduate Research Fellowship Program under Grant No. DGE – 1656518. We thank Charles Musgrave, Joe Berry and Laura Mundt for productive discussions.

Author contributions

Conceptualization: JB, AGP, MFT

Data curation: JB, AGP, JAV

Formal analysis: JB, JAV, LW, NJW, ZZ

Investigation: REB, AFN (sample prep), AGP, JAV, LW, LTS (XRD), EW (EQE)

Methodology: JB, AGP, MFT, JAV, LW, NJW, ZZ

Supervision: LTS, AFN, MDM, MFT

Validation: JAW, LW, NJW, ZZ

Visualisation: JB, ZZ

Writing – original draft: JB, REB

Writing – review & editing: all authors

References

1. Manser JS, Christians JA, and Kamat PV. Intriguing optoelectronic properties of metal halide perovskites. Chemical reviews 2016; 116:12956–3008. DOI: `10.1021/acs.chemrev.6b00136`
2. Fu Y, Zhu H, Chen J, Hautzinger MP, Zhu XY, and Jin S. Metal halide perovskite nanostructures for optoelectronic applications and the study of physical properties. Nature Reviews Materials 2019; 4:169–88. DOI: `10.1038/s41578-019-0080-9`
3. Eperon GE, Leijtens T, Bush KA, Prasanna R, Green T, Wang JTW, McMeekin DP, Volonakis G, Milot RL, and May R. Perovskite-perovskite tandem photovoltaics with optimized band gaps. Science 2016; 354:861–5. DOI: `10.1126/science.aaf9717`
4. Kovalenko MV, Protesescu L, and Bodnarchuk MI. Properties and potential optoelectronic applications of lead halide perovskite nanocrystals. Science 2017; 358:745–50. DOI: `10.1126/science.aam7093`
5. Sahli F, Werner J, Kamino BA, Bräuninger M, Monnard R, Paviet-Salomon B, Barraud L, Ding L, Leon JJD, and Sacchetto D. Fully textured monolithic perovskite/silicon tandem solar cells with 25.2% power conversion efficiency. Nature materials 2018 :1. DOI: `10.1038/s41563-018-0115-4`
6. Xu J, Boyd CC, Zhengshan JY, Palmstrom AF, Witter DJ, Larson BW, France RM, Werner J, Harvey SP, Wolf EJ, et al. Triple-halide wide–band gap perovskites with suppressed phase segregation for efficient tandems. Science 2020; 367:1097–104. DOI: `10.1026/science.aaz5074`
7. NREL. Best research-cell efficiency chart. `https://www.nrel.gov/pv/cell-efficiency.html`. accessed Feb 2021. 2020
8. Green MA, Dunlop ED, Hohl-Ebinger J, Yoshita M, Kopidakis N, and Ho-Baillie AW. Solar cell efficiency tables (Version 55). Progress in Photovoltaics: Research and Applications 2020; 28:3–15. DOI: `10.1002/pip.3371`
9. Correa-Baena JP, Saliba M, Buonassisi T, Grätzel M, Abate A, Tress W, and Hagfeldt A. Promises and challenges of perovskite solar cells. Science 2017; 358:739–44. DOI: `10.1126/science.aam6323`
10. Snaith HJ. Present status and future prospects of perovskite photovoltaics. Nature materials 2018; 17:372–6. DOI: `10.1038/s41563-018-0071-z`
11. Soto-Montero T, Soltanpoor W, and Morales-Masis M. Pressing challenges of halide perovskite thin film growth. APL materials 2020; 8:110903. DOI: `10.1063/5.0027573`
12. Leijtens T, Bush KA, Prasanna R, and McGehee MD. Opportunities and challenges for tandem solar cells using metal halide perovskite semiconductors. Nature Energy 2018; 3:828–38. DOI: `10.1038/s41560-018-0190-4`
13. Hoke ET, Slotcavage DJ, Dohner ER, Bowring AR, Karunadasa HI, and McGehee MD. Reversible photo-induced trap formation in mixed-halide hybrid perovskites for photovoltaics. Chemical Science 2015; 6:613–7. DOI: `10.1039/C4SC03141E`

14. Beal RE, Hagström NZ, Barrier J, Gold-Parker A, Prasanna R, Bush KA, Pasarello D, Schelhas L, Brüning K, Steinrück HG, McGehee MD, Toney MF, and Nogueira AF. Structural origins of light-induced phase segregation in organic-inorganic halide perovskite photovoltaic materials. Matter 2020; 2:1–13. DOI: `10.1016/j.matt.2019.11.001`

15. Knight AJ and Herz LM. Preventing phase segregation in mixed-halide perovskites: a perspective. Energy & Environmental Science 2020; 13:2024–46. DOI: `10.1039/d0ee00788A`

16. Brennan MC, Ruth A, Kamat PV, and Kuno M. Photoinduced anion segregation in mixed halide perovskites. Trends in Chemistry 2020; 2:282–301. DOI: `10.1016/j.trechm.2020.01.010`

17. Eames C, Frost JM, Barnes PR, O'regan BC, Walsh A, and Islam MS. Ionic transport in hybrid lead iodide perovskite solar cells. Nature communications 2015; 6:1–8. DOI: `10.1038/ncomms8497`

18. Walsh A and Stranks SD. Taking control of ion transport in halide perovskite solar cells. ACS Energy Letters 2018; 3:1983–90. DOI: `10.1021/acsenergylett.8b00764`

19. Senocrate A and Maier J. Solid-state ionics of hybrid halide perovskites. Journal of the American Chemical Society 2019; 141:8382–96. DOI: `10.1021/jacs.8b13594`

20. Schelhas LT, Li Z, Christians JA, Goyal A, Kairys P, Harvey SP, Kim DH, Stone KH, Luther JM, Zhu K, et al. Insights into operational stability and processing of halide perovskite active layers. Energy & Environmental Science 2019; 12:1341–8. DOI: `10.1039/C8EE03051K`

21. Bush KA, Frohna K, Prasanna R, Beal RE, Leijtens T, Swifter SA, and McGehee MD. Compositional engineering for efficient wide band gap perovskites with improved stability to photoinduced phase segregation. ACS Energy Letters 2018; 3:428–35. DOI: `10.1021/acsenergylett.7b01255`

22. Barker AJ, Sadhanala A, Deschler F, Gandini M, Senanayak SP, Pearce PM, Mosconi E, Pearson AJ, Wu Y, Srimath Kandada AR, et al. Defect-assisted photoinduced halide segregation in mixed-halide perovskite thin films. ACS Energy Letters 2017; 2:1416–24. DOI: `10.1021/acsenergylett.7b00282`

23. Bischak CG, Sanehira EM, Precht JT, Luther JM, and Ginsberg NS. Heterogeneous Charge Carrier Dynamics in Organic-Inorganic Hybrid Materials: Nanoscale Lateral and Depth-Dependent Variation of Recombination Rates in Methylammonium Lead Halide Perovskite Thin Films. Nano Lett. 2015; 15(7):4799–807. DOI: `10.1021/acs.nanolett.5b01917`

24. Bischak CG, Hetherington CL, Wu H, Aloni S, Ogletree DF, Limmer DT, and Ginsberg NS. Origin of Reversible Photoinduced Phase Separation in Hybrid Perovskites. Nano Lett. 2017; 17:1028–33. DOI: `10.1021/acs.nanolett.6b04453`

25. Bischak CG, Wong AB, Lin E, Limmer DT, Yang P, and Ginsberg NS. Tunable Polaron Distortions Control the Extent of Halide Demixing in Lead Halide Perovskites. J. Phys. Chem. Lett. 2018; 9:3998–4005. DOI: `10.1021/acs.jpclett.8b01512`

26. Wieghold S, Tresback J, Correa-Baena JP, Hartono NTP, Sun S, Liu Z, Layurova M, VanOrman ZA, Bieber AS, Thapa J, Lai B, Cai Z, Nienhaus L, and Buonassisi T. Halide Heterogeneity Affects Local Charge Carrier Dynamics in Mixed-Ion Lead Perovskite Thin Films. Chem. Mater. 2019; 31:3712?3721. DOI: `10.1021/acs.chemmater.9b00650`

27. Quilettes DW de, Vorpahl SM, Stranks SD, Nagaoka H, Eperon GE, Ziffer ME, Snaith HJ, and Ginger DS. Impact of microstructure on local carrier lifetime in perovskite solar cells. Science 2015; 348:683–6. DOI: `10.1126/science.aaa5333`

28. Correa-Baena JP, Luo Y, Brenner TM, Snaider J, Sun S, Li X, Jensen MA, Hartono NTP, Nienhaus L, Wieghold S, et al. Homogenized halides and alkali cation segregation in alloyed organic-inorganic perovskites. Science 2019; 363:627–31. DOI: `10.1126/science.aah5065`

29. Szostak R, Silva J, Turren-Cruz SH, Soares M, Freitas R, Hagfeldt A, Tolentino H, and Nogueira A. Nanoscale mapping of chemical composition in organic-inorganic hybrid perovskite films. Science advances 2019; 5:eaaw6619. DOI: `10.1126/sciadv.aaw6619`

30. Tennyson EM, Doherty TAS, and Stranks SD. Heterogeneity at multiple length scales in halide perovskite semiconductors. Nat. Rev. Mater. 2019; 4:573–87. DOI: `doi.org/10.1038/s41578-019-0125-0`

31. Gratia P, Grancini G, Audinot JN, Jeanbourquin X, Mosconi E, Zimmermann I, Dowsett D, Lee Y, Grätzel M, De Angelis F, et al. Intrinsic halide segregation at nanometer scale determines the high efficiency of mixed cation/mixed halide perovskite solar cells. Journal of the American Chemical Society 2016; 138:15821–4. DOI: `10.1021/jacs.6b10049`

32. Mishra SK, Gupta MK, Mittal R, Zbiri M, Rols S, Schober H, and Chaplot SL. Phonon dynamics and inelastic neutron scattering of sodium niobate. Phys. Rev. B 2014 May; 89(18):184303. DOI: `10.1103/PhysRevB.89.184303`

33. Charles B, Weller MT, Rieger S, Hatcher LE, Henry PF, Feldmann J, Wolverson D, and Wilson CC. Phase Behavior and Substitution Limit of Mixed Cesium-Formamidinium Lead Triiodide Perovskites. Chemistry of Materials 2020; 32:2282–91. DOI: `10.1021/acs.chemmater.9b04032`

34. Mohanty A, Swain D, Govinda S, Row TNG, and Sarma D. Phase Diagram and Dielectric Properties of MA1–x FA x PbI3. ACS Energy Letters 2019; 4:2045–51. DOI: `10.1021/acsenergylett.9b01291`

35. Lehmann F, Franz A, Többens DM, Levcenco S, Unold T, Taubert A, and Schorr S. The phase diagram of a mixed halide (Br, I) hybrid perovskite obtained by synchrotron X-ray diffraction. RSC advances 2019; 9:11151–9. DOI: `10.1039/C8RA09398A`

36. Kim SY, Lee HC, Nam Y, Yun Y, Lee SH, Kim DH, Noh JH, Lee JH, Kim DH, Lee S, and Heo YW. Ternary diagrams of the phase, optical bandgap energy and photoluminescence of mixed-halide perovskites. Acta Materialia 2019; 81:460–9. DOI: `https://doi.org/10.1016/j.actamat.2019.10.008`

37. Li Z, Yang M, Park JS, Wei SH, Berry JJ, and Zhu K. Stabilizing perovskite structures by tuning tolerance factor: formation of formamidinium and cesium lead iodide solid-state alloys. Chemistry of Materials 2016; 28:284–92. DOI: `10.1021/acs.chemmater.5b04107`

38. Bechtel JS and Van der Ven A. First-principles thermodynamics study of phase stability in inorganic halide perovskite solid solutions. Physical Review Materials 2018; 2:045401. DOI: `10.1103/PhysRevMaterials.2.045401`

39. Goldschmidt VM. Die gesetze der krystallochemie. Naturwissenschaften 1926; 14:477–85. DOI: `10.1007/BF01507527`

40. Stokes HT, Kisi EH, Hatch DM, and Howard CJ. Group-theoretical analysis of octahedral tilting in ferroelectric perovskites. Acta Crystallographica Section B 2002 Dec; 58:934–8. DOI: `10.1107/S0108768102015756`

41. Glazer A. The classification of tilted octahedra in perovskites. Acta Crystallographica Section B: Structural Crystallography and Crystal Chemistry 1972; 28:3384–92. DOI: `10.1107/S0567740872007976`

42. Cochran W. Crystal Stability and the Theory of Ferroelectricity. Phys. Rev. Lett. 1959 Nov; 3(9):412–4. DOI: `10.1103/PhysRevLett.3.412`

43. Woodward PM. Octahedral tilting in perovskites. I. Geometrical considerations. Acta Crystallographica Section B 1997; 53:32–43. DOI: `10.1107/S0108768196010713`

44. Woodward PM. Octahedral tilting in perovskites. II. Structure stabilizing forces. Acta Crystallographica Section B 1997; 53:44–66. DOI: `10.1107/S0108768196012050`

45. Aleksandrov K. The sequences of structural phase transitions in perovskites. Ferroelectrics 1976; 14:801–5. DOI: `10.1080/00150197608237799`

46. Bechtel JS and Van der Ven A. Octahedral tilting instabilities in inorganic halide perovskites. Phys. Rev. Materials 2018 Feb; 2(2):025401. DOI: `10.1103/PhysRevMaterials.2.025401`

47. Zhong W and Vanderbilt D. Competing Structural Instabilities in Cubic Perovskites. Phys. Rev. Lett. 1995 Mar; 74(13):2587–90. DOI: `10.1103/PhysRevLett.74.2587`

48. Gopalan V and Litvin DB. Rotation-reversal symmetries in crystals and handed structures. Nature materials 2011; 10:376. DOI: `10.1038/nmat2987`

49. Bartel CJ, Sutton C, Goldsmith BR, Ouyang R, Musgrave CB, Ghiringhelli LM, and Scheffler M. New tolerance factor to predict the stability of perovskite oxides and halides. Science advances 2019; 5:eaav0693. DOI: `10.1126/sciadv.aav0693`

50. Schelhas LT, Christians JA, Berry JJ, Toney MF, Tassone CJ, Luther JM, and Stone KH. Monitoring a silent phase transition in CH3NH3PbI3 solar cells via operando X-ray diffraction. ACS Energy Letters 2016; 1:1007–12. DOI: `10.1021/acsenergylett.6b00441`

51. Cowley RA. Lattice Dynamics and Phase Transitions of Strontium Titanate. Phys. Rev. 1964 May; 134(4A):A981–A997. DOI: `10.1103/PhysRev.134.A981`

52. Shirane G and Yamada Y. Lattice-Dynamical Study of the 110°K Phase Transition in $SrTiO_3$. Phys. Rev. 1969 Jan; 177(2):858–63. DOI: `10.1103/PhysRev.177.858`

53. Harada J, Axe JD, and Shirane G. Neutron-Scattering Study of Soft Modes in Cubic $BaTiO_3$. Phys. Rev. B 1971 Jul; 4(1):155–62. DOI: `10.1103/PhysRevB.4.155`

54. Salje EKH, Gallardo MC, Jiménez J, Romero FJ, and Cerro J del. The cubic-tetragonal phase transition in strontium titanate: excess specific heat measurements and evidence for a near-tricritical, mean field type transition mechanism. Journal of Physics: Condensed Matter 1998 Jun; 10:5535–43. DOI: `10.1088/0953-8984/10/25/006`

55. Young J and Rondinelli JM. Octahedral rotation preferences in perovskite iodides and bromides. The journal of physical chemistry letters 2016; 7:918–22. DOI: `10.1021/acs.jpclett.6b00094`

56. Weber OJ, Ghosh D, Gaines S, Henry PF, Walker AB, Islam MS, and Weller MT. Phase behavior and polymorphism of formamidinium lead iodide. Chemistry of Materials 2018; 30:3768–78. DOI: `10.1021/acs.chemmater.8b00862`

57. Ghosh D, Smith AR, Walker AB, and Islam MS. Mixed a-cation perovskites for solar cells: atomic-scale insights into structural distortion, hydrogen bonding, and electronic properties. Chemistry of Materials 2018; 30:5194–204. DOI: `10.1021/acs.chemmater.8b01851`

58. Francisco-López A, Charles B, Alonso MI, Garriga M, Campoy-Quiles M, Weller MT, and Goñi AR. Phase Diagram of Methylammonium/Formamidinium Lead Iodide Perovskite Solid Solutions from Temperature-Dependent Photoluminescence and Raman Spectroscopies. The Journal of Physical Chemistry C 2020; 124:3448–58. DOI: `10.1021/acs.jpcc.9b10185`

59. Franz A, Többens DM, Lehmann F, Kärgell M, and Schorr S. The influence of deuteration on the crystal structure of hybrid halide perovskites: a temperature-dependent neutron diffraction study of FAPbBr3. Acta Crystallographica Section B: Structural Science, Crystal Engineering and Materials 2020; 76. DOI: `10.1107/S2052520620002620`

60. Kawamura Y, Mashiyama H, and Hasebe K. Structural Study on Cubic?Tetragonal Transition of CH3NH3PbI3. Journal of the Physical Society of Japan 2002; 71:1694–7. DOI: `10.1143/JPSJ.71.1694`

61. Mashiyama H, Kawamura Y, Magome E, and Kubota Y. Displacive Character of the Cubic-Tetragonal Transition in $CH_3NH_3PbX_3$. J. Korean Phy. Soc. 2003 Apr; 42(April):S1026–S1029

62. Comin R, Crawford MK, Said AH, Herron N, Guise WE, Wang X, Whitfield PS, Jain A, Gong X, McGaughey AJH, and Sargent EH. Lattice dynamics and the nature of structural transitions in organolead halide perovskites. Phys. Rev. B 2016 Sep; 94(9):094301. DOI: `10.1103/PhysRevB.94.094301`

63. Whitfield P, Herron N, Guise W, Page K, Cheng Y, Milas I, and Crawford M. Structures, phase transitions and tricritical behavior of the hybrid perovskite methyl ammonium lead iodide. Scientific reports 2016; 6:35685. DOI: `10.1038/srep35685`

64. Brivio F, Frost JM, Skelton JM, Jackson AJ, Weber OJ, Weller MT, Goñi AR, Leguy AMA, Barnes PRF, and Walsh A. Lattice dynamics and vibrational spectra of the orthorhombic, tetragonal, and cubic phases of methylammonium lead iodide. Phys. Rev. B 2015; 92. DOI: `10.1103/PhysRevB.92.144308`

65. Cordero F, Trequattrini F, Craciun F, Paoletti A, Pennesi G, and Zanotti G. Cation reorientation and octahedral tilting in the metal-organic perovskites MAPI and FAPI. Journal of Alloys and Compounds 2020 :158210. DOI: `10.1016/j.jallcom.2020.158210`

66. Weadock NJ, Gehring PM, Gold-Parker A, Smith IC, Karunadasa HI, and Toney MF. On the question of dynamic domains and critical scattering in cubic methylammonium lead triiodide. Physical Review Letters 2020; 125:075701. DOI: `10.1103/PhysRevLett.125.075701`

67. Ru N, Condron C, Margulis G, Shin K, Laverock J, Dugdale S, Toney M, and Fisher I. Effect of chemical pressure on the charge density wave transition in rare-earth tritellurides R Te 3. Physical Review B 2008; 77:035114. DOI: `10.1103/PhysRevB.77.035114`

68. Abdelsamie M, Xu J, Bruening K, Tassone CJ, Steinrück HG, and Toney MF. Impact of Processing on Structural and Compositional Evolution in Mixed Metal Halide Perovskites during Film Formation. Advanced Functional Materials 2020 Jul; 30:2001752. DOI: `10.1002/adfm.202001752`

69. Chang Y, Park C, and Matsuishi K. First principles study of the structural and the electronic properties of the lead-halide-based inorganic-organic perovskites $(CH_3NH_3)PbX_3$ and $CsPbX_3$ (X = Cl, Br, I). Journal of the Korean Physical Society 2004; 44(4):889–93

70. Grote C and Berger RF. Strain tuning of tin–halide and lead–halide perovskites: a first-principles atomic and electronic structure study. The Journal of Physical Chemistry C 2015; 119:22832–7. DOI: `10.1021/acs.jpcc.5b07446`

71. Lee JH, Bristowe NC, Lee JH, Lee SH, Bristowe PD, Cheetham AK, and Jang HM. Resolving the physical origin of octahedral tilting in halide perovskites. Chemistry of Materials 2016; 28:4259–66. DOI: `10.1021/acs.chemmater.6b00968`

72. Prasanna R, Gold-Parker A, Leijtens T, Conings B, Babayigit A, Boyen HG, Toney MF, and McGehee MD. Band gap tuning via lattice contraction and octahedral tilting in perovskite materials for photovoltaics. Journal of the American Chemical Society 2017; 139:11117–24. DOI: `10.1021/jacs.7b04981`

73. Bokov AA and Ye ZG. Recent progress in relaxor ferroelectrics with perovskite structure. Journal of Materials Science 2006; 41:31–52

74. Mozur EM, Hope MA, Trowbridge JC, Halat DM, Daemen LL, Maughan AE, Prisk TR, Grey CP, and Neilson JR. Cesium Substitution Disrupts Concerted Cation Dynamics in Formamidinium Hybrid Perovskites. Chemistry of Materials 2020; 32:6266–77

75. Simenas M, Balciunas S, Wilson JN, Svirskas S, Kinka M, Garbaras A, Kalendra V, Gagor A, Szewczyk D, Sieradzki A, et al. Suppression of phase transitions and glass phase signatures in mixed cation halide perovskites. Nature communications 2020; 11:1–9

76. Kieffer J and Karkoulis D. PyFAI, a versatile library for azimuthal regrouping. *Journal of Physics: Conference Series*. IOP Publishing. 2013 :202012. DOI: `10.1088/1742-6596/425/20/202012i`

77. Sheldrick GM. SHELXT–Integrated space-group and crystal-structure determination. Acta Crystallographica Section A: Foundations and Advances 2015; 71:3–8. DOI: `10.1107/S2053273314026370`